


## High-throughput screening for spin-gapless semiconductors in quaternary Heusler compounds

Qiang Gao, Ingo Opahle, and Hongbin Zhang\*

*Institute of Materials Science, Technische Universität Darmstadt, 64287 Darmstadt, Germany*

 (Received 1 August 2018; revised manuscript received 14 December 2018; published 27 February 2019)

Based on high-throughput density functional theory calculations, we performed a systematic screening for spin-gapless semiconductors (SGSs) in quaternary Heusler alloys  $XX'YZ$  ( $X$ ,  $X'$ , and  $Y$  are transition metal elements except Tc, and  $Z$  is one of B, Al, Ga, In, Si, Ge, Sn, Pb, P, As, Sb, and Bi). Following an empirical rule, we focused on compounds with 21, 26, or 28 valence electrons, resulting in 12 000 possible chemical compositions. After systematically evaluating the thermodynamic, mechanical, and dynamical stabilities, we have identified 70 so far unreported SGSs, confirmed by explicit electronic structure calculations with proper magnetic ground states, of which 17 candidates have a distance to the convex hull smaller than 0.10 eV/atom. It is demonstrated that all four types of SGSs can be realized, defined based on the spin characters of the bands around the Fermi energy. Type-II SGSs show promising transport properties for spintronic applications. The effect of spin-orbit coupling is investigated, resulting in large anisotropic magnetoresistance and anomalous Nernst effects.

DOI: [10.1103/PhysRevMaterials.3.024410](https://doi.org/10.1103/PhysRevMaterials.3.024410)

### I. INTRODUCTION

In recent years, spin-gapless semiconductors (SGSs) have drawn intensive attention to the spintronics community. Conventional SGSs are half metals with the majority-spin channel being semimetallic, i.e., the gap is zero, while there is a finite band gap in the minority-spin channel. Following Ref. [1], four types of SGSs can be defined based on the spin character of the bands around the Fermi energy as sketched in Fig. 1(a). In the type-I SGSs, the valence band maximum (VBM) and conduction band minimum (CBM) are in the same spin channel while there is a gap in the opposite spin channel. This is the conventional SGS mentioned above. Moreover, the CBM and VBM can hold opposite spin characters, hereafter dubbed type-II SGSs. Additionally, if the VBM (CBM) is of one spin character while the CBMs (VBMs) originate from both spin channels, type-III (type-IV) SGSs will be defined. In principle, the VBM and CBM can touch each other at the same or different  $k$  points, corresponding to the direct or indirect zero band gap. In comparison to the usual half metals, the 100% spin-polarized carriers can be excited from the valence to conduction bands with no energy cost, leading to new functionalities and potential applications in logic gates. For instance, the spin-polarized transport properties of SGSs can be tuned by shifting the Fermi energy with finite gate voltages [1,2], which is promising for future spintronic applications.

Based on first-principles calculations, it was originally proposed that Co-doped  $\text{PbPdO}_2$  can host the SGS state [1]. However, its Curie temperature ( $T_C$ ) is just about 180 K [3], well below room temperature. The first above-room-temperature SGS was experimentally observed in the inverse Heusler  $\text{Mn}_2\text{CoAl}$  ( $T_C = 720$  K) [2]. Later on, the Heusler compounds were considered outstanding candidates for SGSs.

For example, ternary Heusler  $\text{Ti}_2\text{MnAl}$ , quaternary Heusler  $\text{CoFeMnSi}$ , and  $\text{DO}_3$ -type Heusler  $\text{V}_3\text{Al}$  were predicted theoretically to be SGSs [4–6] and also confirmed by experimental measurements [7–9]. Interestingly, during the explorations of SGSs in the Heusler compounds, an empirical rule was discovered. That is, the Heusler compounds with 18, 21, 26, or 28 valence electrons are more likely to realize the SGS phase [4,10,11]. However, there has been no systematic study to design novel SGS Heusler systems. Particularly, there are still a few questions about SGSs to be understood. For instance, all four types of SGSs should in principle exist but most experimentally studied systems are of type I and type II [4,5,10]. A particularly intriguing question is the effect of spin-orbit coupling (SOC) on the transport properties of SGSs, i.e., whether a band gap can be opened with nontrivial topological properties. Wang has proposed recently that SGSs are promising for massless and dissipationless spintronics and quantum anomalous Hall effects [12]. In this regard, SGSs with direct band touching will be very interesting, since they may host nontrivial topological properties after considering SOC.

On the other hand, high-throughput (HTP) screening based on density functional theory (DFT) calculations has been proven to be an efficient way to search for materials with desired properties [13,14]. Using the AFLOWLIB database, Carrete *et al.* have done HTP calculations on approximately 79 000 half-Heusler compounds and found 75 systems which are thermodynamically stable, where the thermal conductivities and thermoelectric performance have also been evaluated [15]. The Heusler compounds with ten valence electrons ( $X_2YZ$ ,  $X = \text{Ca, Sr, and Ba}$ ;  $Y = \text{Au}$ ;  $Z = \text{Sn, Pb, As, Sb, and Bi}$ ) are demonstrated to have ultralow lattice thermal conductivities according to He's HTP calculations [16]. In a more recent HTP study, He *et al.* have identified 99 new non-magnetic semiconductors following the 18 valence electron rule with promising thermoelectric properties [17]. Furthermore, for spintronic applications, Ma *et al.* have performed a

\*Corresponding author: [h Zhang@tmm.tu-darmstadt.de](mailto:h Zhang@tmm.tu-darmstadt.de)

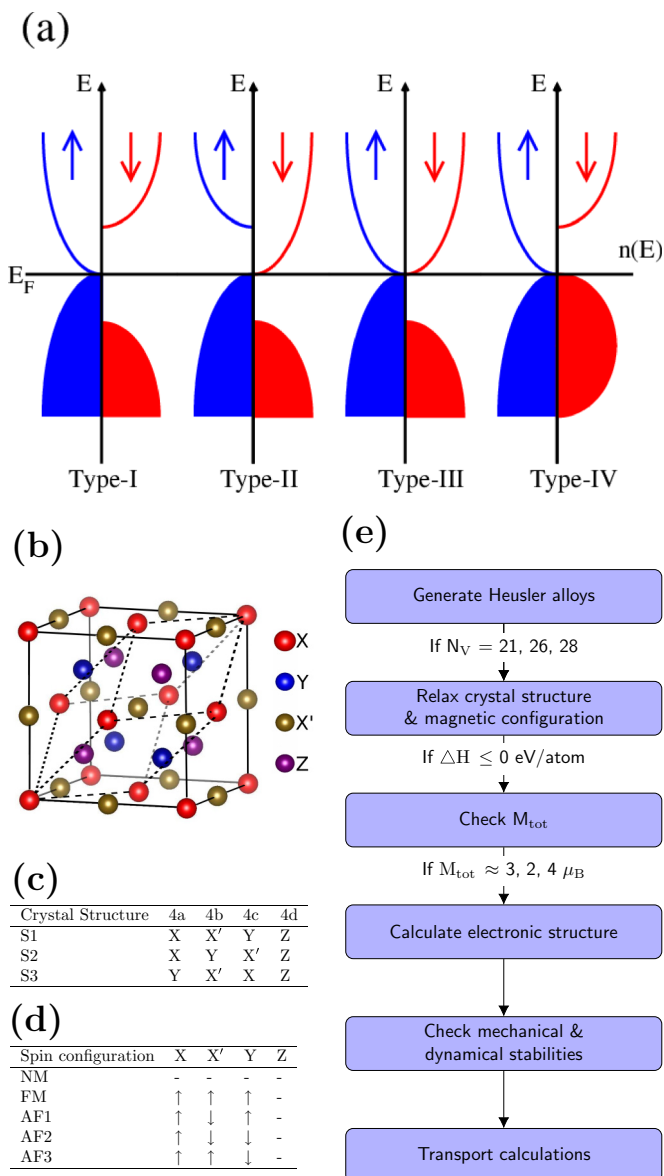


FIG. 1. (a) Sketches of the density of states for the four types of SGs, defined based on the touching schemes of the majority (marked in blue) and minority (marked in red) bands. (b) The crystal structure of quaternary Heusler  $XX'YZ$ , where the solid (dashed) lines indicate the conventional cubic (primitive rhombohedral) cell. (c) The three possible site occupations for a quaternary Heusler alloy with a specific chemical composition. (d) The possible spin configurations within the primitive cell. (e) The work flow for the present HTP screening.

systemic HTP study on 405 inverse Heusler alloys resulting in 14 stable semiconductors and 10 half metals [18]. Focusing on the magnetic properties, Sanvito *et al.* did HTP calculations on 36 540 Heusler alloys, leading to 248 thermodynamically stable compounds with 20 magnetic cases [19]. Moreover, 21 antiferromagnetic Heusler compounds with high Néel temperature have been proposed for spintronic applications [20]. Last but not least, among 286 Heusler compounds, HTP screening calculations suggest 62% have a tetragonal structure due to the peak-and-valley character in the density of states [21].

In this work, we have carried out a systematic HTP screening for SGs in Heusler compounds (including  $DO_3$  binary, ternary, and quaternary Heusler systems). Based on the empirical rule, we considered 12 000 systems with 21, 26, or 28 valence electrons and identified 80 novel SGs, which are thermodynamically stable based on the formation energies. Among them, 70 are both mechanically and dynamically stable. It is noted that the Heusler alloys with 18 valence electrons are also promising for realizing SGs [4,7,22], which will be investigated in the future. We have identified all four types of SGs in the quaternary Heusler compounds, together with one case showing direct band touching at the Fermi energy. The longitudinal and transversal transport properties were also evaluated based on the semiclassical transport theory, revealing that SGs are promising materials for spintronic applications. It is demonstrated that the magnetization direction can be used to tailor the electronic structure and hence the physical properties for SGs with heavy elements, due to the anisotropy caused by SOC.

## II. COMPUTATIONAL DETAILS

We considered quaternary Heusler compounds with a general chemical formula  $XX'YZ$ , where  $X$ ,  $X'$ , and  $Y$  are transition metal elements except for the radioactive Tc, and  $Z$  is one of the main group elements among B, Al, Ga, In, Si, Ge, Sn, Pb, P, As, Sb, and Bi. For convenience, the ternary and binary ( $DO_3$ -type) Heusler systems are considered as quaternary Heusler by allowing  $X$ ,  $X'$ , or  $Y$  to be the same element. As shown in Fig. 1(b), quaternary Heusler  $XX'YZ$  has the so-called LiMgPdSn-type structure with space group  $F\bar{4}3m$  (space group 216), consisting of 4 Wyckoff positions  $4a(0,0,0)$ ,  $4c(\frac{1}{4}, \frac{1}{4}, \frac{1}{4})$ ,  $4b(\frac{1}{2}, \frac{1}{2}, \frac{1}{2})$ , and  $4d(\frac{3}{4}, \frac{3}{4}, \frac{3}{4})$  [23,24]. According to the empirical rule for the number of valence electrons ( $N_V$ ), all the possible chemical composition with 21, 26, and 28 valence electrons are generated, leading to about 12 000 possible compounds. Moreover, three site occupations are considered for each chemical composition, as shown in Fig. 1(c) [25]. Lastly, we consider that all the transition metal elements ( $X$ ,  $X'$ , and  $Y$ ) are magnetic while the main group element ( $Z$ ) is nonmagnetic (NM). For each chemical composition in each site occupation, we consider five spin configurations, namely, the NM, FM, AF1, AF2, and AF3 phases [Fig. 1(d)].

The HTP screening has been carried out in an automated way following the work flow shown in Fig. 1(e), managed with our in-house-developed high-throughput environment (HTE) [14,26]. The DFT calculations are performed using the Vienna *ab initio* Simulation Package (VASP) [27,28]. For each composition-occupation case, the structural relaxation is done in a two-step manner to save computational time. In the first step, ultrasoft pseudopotentials [29] are used in combination with the PW91 [30] exchange correlation functional, where the cutoff energy for the plane wave basis is set to 250 eV and a  $k$ -space density of  $30 \text{ \AA}^{-1}$ . The follow-up finer relaxation is done using the projector augmented plane wave (PAW) method with the exchange-correlation functional under the generalized gradient approximation (GGA) parametrized by Perdew, Burke, and Ernzerhof (PBE) [31]. The cutoff energy for the plane wave expansion is increased to 350 eV and

the  $k$ -mesh density is increased to  $40 \text{ \AA}^{-1}$  to achieve good convergence. The structural relaxations are done for each magnetic configuration mentioned above.

After obtaining the magnetic ground state together with the optimized crystalline structures, the formation energy ( $\Delta H$ ) is evaluated to verify the thermodynamic stability, i.e., the stability with respect to decomposing into constituting elements. For a general quaternary Heusler  $XX'YZ$ , the formation energy is expressed as

$$\Delta H^{XX'YZ} = \frac{1}{4}[E^{XX'YZ} - (E^X + E^{X'} + E^Y + E^Z)], \quad (1)$$

where  $E^X$ ,  $E^{X'}$ ,  $E^Y$ , and  $E^Z$  are the energies of elements  $X$ ,  $X'$ ,  $Y$ , and  $Z$  in their bulk forms, while  $E^{XX'YZ}$  is the ground state energy of  $XX'YZ$ . In addition, we also evaluated the distances to the convex hull based on the Open Quantum Materials Database (OQMD) [32].

The electronic structure together with the magnetic moments of the compounds with negative formation energies are calculated with a denser  $k$  mesh of  $21 \times 21 \times 21$  using the full-potential local-orbital minimum-basis band structure scheme (FPLO) [33,34]. The SGS phase can be identified by examining the value of magnetic moments (i.e., being an integer following the Slater-Pauling rule as discussed below) and the band structure directly.

For the candidate SGSs, we further checked the mechanical and dynamical stability. The mechanical stability describes the stability of the crystal against deformations or distortions in terms of strain, which can be obtained based on the elastic constants ( $C_{ij}$ ). The elastic constants are associated with the second-order change of the internal energy for a crystal under an arbitrary deformation of strain as

$$C_{ij} = \frac{1}{V_0} \left( \frac{\partial^2 E}{\partial \varepsilon_i \partial \varepsilon_j} \right), \quad (2)$$

where  $E$  is the internal energy,  $V_0$  is the equilibrium volume of the crystal, and  $\varepsilon_i$  or  $\varepsilon_j$  denote applied strains. For a cubic crystal system (such as Heusler compounds in this work), the elastic constant matrix has only three independent elements as

$$C_{\text{cubic}} = \begin{bmatrix} C_{11} & C_{12} & C_{12} & 0 & 0 & 0 \\ C_{12} & C_{11} & C_{12} & 0 & 0 & 0 \\ C_{12} & C_{12} & C_{11} & 0 & 0 & 0 \\ 0 & 0 & 0 & C_{44} & 0 & 0 \\ 0 & 0 & 0 & 0 & C_{44} & 0 \\ 0 & 0 & 0 & 0 & 0 & C_{44} \end{bmatrix}. \quad (3)$$

Correspondingly, the Born stability conditions [35] suggest

$$C_{11} + 2C_{12} > 0, \quad C_{11} - C_{12} > 0, \quad C_{44} > 0, \quad (4)$$

which are related to the bulk, tetragonal, and shear moduli, respectively.

On the other hand, the dynamical stability describes the change of the total energy with respect to the internal degrees of freedom, i.e., the atomic displacements. In the harmonic approximation, the total energy of a crystal can be expressed as in terms of displacements  $D_{\mathbf{R}\sigma}$ ,

$$E = E_0 + \frac{1}{2} \sum_{\mathbf{R}, \sigma} \sum_{\mathbf{R}', \sigma'} D_{\mathbf{R}\sigma} \Phi_{\mathbf{R}\mathbf{R}'}^{\sigma\sigma'} D_{\mathbf{R}'\sigma'}, \quad (5)$$

where  $\mathbf{R}$  is the position,  $\sigma$  is the Cartesian index, and  $\Phi_{\mathbf{R}\mathbf{R}'}^{\sigma\sigma'}$  is the interatomic force constant matrix. The dynamical stability is determined by the dynamical matrix  $D(\mathbf{q})$ , which can be obtained from Fourier transformation of  $\Phi(\mathbf{R})$  as follows:

$$D(\mathbf{q}) = \frac{1}{M} \sum_{\mathbf{R}} \Phi(\mathbf{R}) e^{-i\mathbf{q}\mathbf{R}}, \quad (6)$$

where  $\mathbf{q}$  is the wave vector of phonon. Dynamical stability indicates that  $D(\mathbf{q})$  is positive-definite, meaning all the phonons have real and positive frequencies  $\omega(\mathbf{q})$ . The phonon dispersion calculations are carried out using the Phonopy [36] package with force constants obtained from VASP.

Finally, the transport properties are studied for a few representative SGS candidates, including the anomalous Hall conductivity (AHC) and the longitudinal conductivity. The AHC is calculated by integrating the Berry curvature [ $\Omega(\mathbf{k})$ ] over the whole Brillouin zone (BZ) as  $\sigma_{xy} = \frac{e^2}{\hbar} \int_{\text{BZ}} \Omega(\mathbf{k}) d^3\mathbf{k}$ , with the Berry curvature given by

$$\Omega_{xy}(\mathbf{k}) = 2\text{Im} \sum_{\epsilon_{n\mathbf{k}}, \epsilon_{m\mathbf{k}} \leq E_F} \sum_{m \neq n} \frac{\langle \psi_{n\mathbf{k}} | v_x | \psi_{m\mathbf{k}} \rangle \langle \psi_{m\mathbf{k}} | v_y | \psi_{n\mathbf{k}} \rangle}{(\epsilon_{m\mathbf{k}} - \epsilon_{n\mathbf{k}})^2}, \quad (7)$$

where  $\psi_{\alpha\mathbf{k}}$  is the spinor Bloch wave function corresponding to the eigenenergy  $\epsilon_{\alpha\mathbf{k}}$ , and  $v_i$  is the  $i$ th Cartesian component of the velocity operator. In our calculations, in order to achieve numerical convergence, the AHC is obtained using the Wannier interpolation technique based on the maximally localized Wannier functions [37]. Furthermore, the longitudinal conductivities at finite temperature (300 K) for SGSs are calculated based on the semiclassical theory with the BoltzTrap [38] code. Here the energy-independent relaxation time ( $\tau$ ) is used to approximate the distribution function as

$$\left( \frac{\partial f}{\partial t} \right)_s = -\frac{f - f_0}{\tau}, \quad (8)$$

where  $f_0$  and  $f$  are the equilibrium and nonequilibrium distribution functions, respectively. The conductivity is expressed by

$$\sigma_{\alpha\beta}(T, \mu) = \frac{1}{V} \int \bar{\sigma}_{\alpha\beta}(\epsilon) \left[ -\frac{\partial f_0(T, \epsilon, \mu)}{\partial \epsilon} \right] d\epsilon, \quad (9)$$

where  $\alpha$  and  $\beta$  are the Cartesian indices, and  $V$  and  $\mu$  indicate the unit cell volume and the chemical potential, respectively. The transport distribution function  $\bar{\sigma}_{\alpha\beta}(\epsilon)$  can be evaluated by

$$\bar{\sigma}_{\alpha\beta}(\epsilon) = \frac{e^2}{N} \sum_{i, \mathbf{k}} \tau \cdot v_{\alpha}(i, \mathbf{k}) \cdot v_{\beta}(i, \mathbf{k}) \cdot \frac{\delta(\epsilon - \epsilon_{i, \mathbf{k}})}{d\epsilon}, \quad (10)$$

$$v_{\alpha}(i, \mathbf{k}) = \frac{1}{\hbar} \nabla_{\mathbf{k}} \epsilon_{i, \mathbf{k}}, \quad (11)$$

where  $\mathbf{k}$ ,  $i$ , and  $N$  are the wave vector, band index, and the number of the sampled  $\mathbf{k}$  points. For bonding analysis, the crystal orbital Hamilton population (COHP) was evaluated using the LOBSTER code [39].

### III. RESULTS AND DISCUSSION

#### A. HTP search validation

To validate our HTP scheme, we collected previously reported Heusler SGSs, and compared with our DFT results (Table I). The lattice constants, total magnetic moments

TABLE I. Comparisons between our HTP calculations and previous reported SGSs. For the mechanical and dynamical stabilities, “1” (“0”) indicates the system is stable (unstable). “Ref. Exp.” and “Ref. Cal.” denote experimental and computational references. The latt.,  $\Delta H$ , and  $\Delta E_{\text{con}}$  are the lattice constant, formation energy, and distance to the convex hull per atom. “Dyn. sta.” and “Mec. sta.” mean dynamical and mechanical stabilities.

Compound	latt. (Å)	$M_{\text{tot}}$ ( $\mu_B$ )	$\Delta H$ (eV/at.)	Mec. sta.	Dyn. sta.	$\Delta E_{\text{con}}$ (eV/at.)
$N_V = 21$						
Ti <sub>2</sub> CoSi	6.081	3.00	-0.3718	0	1	0.3222
Ref. Cal. [4]	6.030	3.03				
MnCrTiSi	5.855	3.02	-0.4103	1	1	0.1237
Ref. Cal. [40]	5.860	2.98				
MnCrVAl	5.897	3.00	-0.2110	1	1	0.0023
Ref. Cal. [40]	5.900	2.99				
MnVTiAs	5.978	2.90	-0.2353	1	1	0.3807
Ref. Cal. [40]	5.990	2.87				
CoVTiAl	5.978	3.00	-0.3248	1	1	0.1032
Ref. Cal. [40]	6.040	3.00				
FeVTiSi	5.978	3.02	-0.4351	1	1	0.1899
Ref. Cal. [40]	5.910	2.99				
FeCrTiAl	5.964	3.02	-0.2920	1	1	0.0720
Ref. Cal. [40]	5.970	3.00				
CoVHfGa	6.193	2.95	-0.2434	1	1	0.1916
Ref. Cal. [41]	6.260	3.00				
CrFeHfGa	6.127	3.00	-0.1858	1	1	0.1252
Ref. Cal. [41]	6.261	3.02				
ZrCoVIn	6.445	2.97	-0.0632	0	1	0.2468
Ref. Cal. [10]	6.468	3.00	-0.3500			
ZrFeCrIn	6.408	3.02	0.0279	1	0	0.2419
Ref. Cal. [10]	6.419	3.00	-0.0325			
ZrFeCrGa	6.177	3.00	-0.1690	1	1	0.1580
Ref. Cal. [10]	6.184	3.00	-0.2400			
ZrFeVGe	6.199	3.06	-0.2069	1	0	0.2691
Ref. Cal. [10]	6.210	3.00	-0.2500			
$N_V = 26$						
Mn <sub>2</sub> CoAl	5.729	2.01	-0.2666	1	1	0.0404
Ref. Exp. [2]	5.798	2.00				
Ref. Cal. [42]	5.760	2.00				
CoFeCrAl	5.692	2.00	-0.1931	1	1	0.1139
Ref. Exp. [43]	5.736	2.00				
Ref. Cal. [44]	5.710	2.00	-0.2500			
CoFeCrGa	5.717	2.00	-0.0686	1	1	0.0984
Ref. Exp. [45]	5.736	2.00				
Ref. Cal. [44]	5.730	2.00				
CoFeTiAs	5.835	2.00	-0.3615	1	1	0.2895
Ref. Cal. [40]	5.850	1.99				
CoMnCrSi	5.669	2.00	-0.3280	1	1	0.0710
Ref. Cal. [5]	5.630	2.00	-0.3750			
FeMnCrSb	6.059	2.00	0.0996	1	1	0.2896
Ref. Cal. [5]	5.980	2.00				
ZrCoFeP	5.941	2.00	-0.3491	0	0	0.5949
Ref. Cal. [10]	5.944	2.00	-0.6500			
$N_V = 28$						
CoFeMnSi	5.597	4.00	-0.3833	1	1	0.0137
Ref. Exp. [8]	5.658	4.00				
Ref. Cal. [46]	5.609	4.00				
Mn <sub>2</sub> CuAl	5.710	0.00	-0.1066	0	0	0.0454
Ref. Cal. [47]	5.650	0.00				

TABLE I. (Continued.)

Compound	latt. (Å)	$M_{\text{tot}}$ ( $\mu_B$ )	$\Delta H$ (eV/at.)	Mec. sta.	Dyn. sta.	$\Delta E_{\text{con}}$ (eV/at.)
Cr <sub>2</sub> ZnSi	5.972	0.00	0.08745	1	0	0.3500
Ref. Cal. [48]	5.850	0.00				
Cr <sub>2</sub> ZnGe	6.123	0.00	0.1898	1	1	0.2750
Ref. Cal. [48]	6.140	0.22				
Cr <sub>2</sub> ZnSn	6.413	0.00	0.3079	1	0	0.3079
Ref. Cal. [48]	6.530	0.14				

(Table I), and the electronic structure (not shown) are in good agreement with the literature. However, even though the formation energies for most of the reported Heusler SGSs are negative, ZrFeCrIn and Cr<sub>2</sub>ZnX (X = Si, Ge, and Sn) turn out to be thermodynamically unstable in our HTP calculations. For ZrFeCrIn, in the previous calculations [10], the energies of composite elements with the fcc structure are considered, which leads to an underestimation of the formation energy. This explains also the big difference for the formation energy of ZrCoVIn. For the Cr<sub>2</sub>ZnX (X = Si, Ge, and Sn) compounds, only the inverse Heusler structure is considered in Ref. [48]. According to our calculations, for all three compounds, an antiferromagnetic metallic configuration in the full Heusler structure is energetically preferable, but the formation energies are still positive. Clearly, even though the electronic structure might be interesting with the hypothetical crystal structures, the stability should be checked before making valid predictions.

For quaternary compounds, the thermodynamical stability with respect to other competing binary, ternary, and quaternary phases, i.e., the distance to the convex hull, should also be evaluated. We note that 55 previously unknown, thermodynamically stable (low convex hull) quaternary Heusler compounds are discovered among 2 000 000 compounds by using a machine-learning method [49]. Moreover we evaluate the distances to the convex hull. As shown in Table I, for the experimentally synthesized cases, CoFeCrAl and CoFeCrGa have distances to the convex hull of 0.1139 and 0.0984 eV/atom, respectively. As reported, CoFeCrAl and CoFeCrGa are stable in partially disordered and ordered phases [43,45,50], respectively. This suggests that quaternary Heusler compounds with a distance to the convex hull of 0.10 eV/atom can still be synthesized. On the other hand, Mn<sub>2</sub>CoAl has a small convex hull of 0.0404 eV/atom, and CoFeMnSi is the most stable one with respect to the competing phases as its distance to the convex hull is just 0.0137 eV/atom. In this regard, we suspect that MnCrVAl, CoVTiAl, FeCrTiAl, CoMnCrSi, and Mn<sub>2</sub>CuAl from previous theoretical calculations are more likely to be synthesized.

Furthermore, it is observed that the mechanical stability or the dynamical stability criteria are also critical for some previously predicted compounds. For instance, according to our calculations, Ti<sub>2</sub>CoSi and ZrCoVIn are mechanically unstable, ZrFeVGe is dynamically unstable, and ZrCoFeP and Mn<sub>2</sub>CuAl are both mechanically and dynamically unstable. We note that such compounds may still be synthesized experimentally using molecular beam epitaxy, which is known



TABLE II. Basic information on the newly predicted SGS candidates with negative formation energies ( $\Delta H$ ). Candidates with a distance to the convex hull ( $\Delta E_{\text{con}}$ ) less than 0.10 eV/atom are highlighted in bold. The compounds with symbol  $\dagger$  are either dynamically or mechanically unstable.

$XX'YZ$ (4a,4b,4c,4d)	latt. (Å)	$M_{\text{tot}}$ ( $\mu_B$ )	$\Delta H$ (eV/atom)	$\Delta E_{\text{con}}$ (eV/atom)	SGS type	$XX'YZ$ (4a,4b,4c,4d)	latt. (Å)	$M_{\text{tot}}$ ( $\mu_B$ )	$\Delta H$ (eV/atom)	$\Delta E_{\text{con}}$ (eV/atom)	SGS type
$N_V = 21$						$N_V = 26$					
IrVYSn	6.720	3.00	-0.0942	0.5628	SOC-I	CoOsTiSb	6.255	2.00	-0.1635	0.3515	I
CoVYSn	6.620	3.00	-0.0862	0.3848	II	CoFeHfSb	6.232	2.00	-0.2847	0.2523	I
CoVScSn	6.402	3.00	-0.2049	0.2221	III	CoOsZrSb	6.453	2.00	-0.1075	0.4645	I
IrVScSn	6.518	3.00	-0.2488	0.4052	SOC-II	RhFeTiSb	6.259	1.95	-0.3896	0.1104	I
RhVScSn	6.518	3.00	-0.2773	0.3527	I	CoFeTiSb	6.074	2.00	-0.2948	0.2202	I
CoVYGe	6.377	3.00	-0.0763	0.4697	II	IrFeTiSb	6.287	1.99	-0.2932	0.3108	III
CoVScGe	6.145	3.00	-0.2749	0.2931	II	CoRuTiSb	6.228	2.00	-0.3261	0.1889	I
IrVScGe	6.300	3.00	-0.3025	0.4045	II	CoFeNbGe	5.961	2.00	-0.2374	0.1506	I
RhVScGe	6.290	3.00	-0.3318	0.4502	II	CoOsNbSn $\dagger$	6.352	2.00	-0.0609	0.2091	I
RhVYGe	6.512	3.00	-0.1377	0.5663	III	CoRuTaSn $\dagger$	6.303	2.00	-0.1268	0.1852	I
CoVYSi	6.297	3.00	-0.1077	0.4701	II	IrFeTaSn	6.354	1.98	-0.1782	0.2328	I
CoVScSi	6.058	3.00	-0.3550	0.2990	II	CoOsTaGe	6.143	2.00	-0.0702	0.3048	I
IrVScSi	6.215	3.00	-0.4254	0.4096	SOC-II	CoOsTaSi $\dagger$	6.064	1.99	-0.2546	0.2234	I
RhVScSi	6.210	3.00	-0.4242	0.4628	II	CoOsTaSn	6.332	2.00	-0.007	0.2413	I
RhVYSi	6.438	3.00	-0.1862	0.6398	III	CoFeTaGe	5.938	2.00	-0.2475	0.1275	I
PtVScAl	6.369	3.00	-0.4431	0.2869	SOC-I	CoFeTaSi	5.856	2.00	-0.4222	0.1275	I
PtVYAl	6.608	3.00	-0.2477	0.5013	I	<b>CoFeTaSn</b>	6.154	2.00	-0.1522	0.0898	I
PtVYGa	6.600	3.00	-0.1867	0.5733	I	<b>IrCoNbAl</b>	6.162	1.99	-0.5563	0.0277	I
<b>FeCrHfAl</b>	6.142	3.00	-0.2456	0.0504	II	<b>IrCoNbGa</b>	6.173	2.00	-0.4043	0.0097	I
<b>OsCrHfAl</b>	6.299	3.00	-0.403	0.0530	II	IrCoNbIn	6.360	2.00	-0.1326	0.1544	I
<b>RuCrHfAl</b>	6.284	3.00	-0.4544	0.0666	II	<b>IrCoTaAl</b>	6.140	2.00	-0.5579	0.0631	I
<b>FeCrTiAl</b>	5.964	3.00	-0.292	0.0504	II	IrCoTaGa $\dagger$	6.150	2.00	-0.4200	0.0370	I
<b>FeCrZrAl</b>	6.194	3.00	-0.2156	0.0914	III	IrCoTaIn $\dagger$	6.336	2.00	-0.1622	0.1768	I
<b>OsCrZrAl</b>	6.347	3.00	-0.3543	0.0617	SOC-II	CoCoNbAl $\dagger$	5.970	2.00	-0.4312	0.0082	I
<b>RuCrZrAl</b>	6.335	3.00	-0.4154	0.0626	III	CoCoNbGa $\dagger$	5.968	2.00	-0.3299	0.0001	I
FeCrScSi	5.992	3.00	-0.279	0.2400	II	CoCoNbIn $\dagger$	6.179	2.00	-0.0869	0.0331	I
FeCrScSn	6.364	3.00	-0.0891	0.2309	II	IrCoTiPb	6.380	2.00	-0.0571	0.3829	I
FeCrYSi	6.236	3.00	-0.0081	0.4739	III	IrCoTiSn	6.276	2.00	-0.3789	0.1461	I
OsCrYSi	6.386	3.00	-0.0246	0.4860	SOC-III	<b>IrCoTiSi</b>	5.965	2.00	-0.6805	0.0785	I
CoVHfAl	6.211	3.00	-0.2896	0.1134	I	CoRuCrAl $\dagger$	5.848	2.01	-0.2802	0.0558	II
IrVHfAl	6.346	3.00	-0.4634	0.1596	II	NiCrMnAl	5.809	2.00	-0.2127	0.1173	III
RhVHfAl	6.342	3.00	-0.3855	0.2355	II	NiReCrAl	5.920	1.97	-0.1633	0.2177	II
CoVZrAl	6.258	3.00	-0.2662	0.1408	I	<b>CoOsCrAl</b>	5.866	2.00	-0.2412	0.0688	II
CoVZrGa	6.238	3.00	-0.2317	0.2233	I	$N_V = 28$					
IrTiZrSn $\dagger$	6.651	2.98	-0.3335	0.3965	II	<b>NiFeMnAl</b>	5.731	4.00	-0.2773	0.0577	IV
IrTiZrSi	6.385	2.96	-0.4232	0.4778	II	Continue with $N_V = 21$					
FeVNbAl	6.117	2.99	-0.2012	0.1238	II	<b>MnCrNbAl</b>	6.077	3.00	-0.1912	0.0228	II
<b>FeVTaAl</b>	6.097	2.99	-0.2202	0.0958	II	<b>MnCrTaAl</b>	6.053	2.99	-0.2124	0.0256	II
MnCrZrGe	6.157	2.99	-0.1473	0.2687	II	FeVHfGe	6.158	3.00	-0.2094	0.2646	II
MnCrZrSi	6.076	3.00	-0.2569	0.2621	II	FeVHfSi	6.079	3.00	-0.3187	0.2753	II
MnCrZrSn	6.393	3.00	-0.0593	0.2317	II	FeVHfSn	6.386	3.00	-0.129	0.1580	II

to be efficient in obtaining metastable crystalline phases. For all the systems which have been experimentally synthesized, such as CoFeCrAl, CoFeCrGa, CoFeMnSi, and Mn<sub>2</sub>CoAl, we observed that they fulfill all three stability criteria based on our calculations. This confirms the reliability of our theoretical framework to do HTP screening for novel SGSs.

### B. New SGS candidates

In the previous section we have shown that our high-throughput approach is suitable to identify realistic SGS candidates reported in the literature. We now proceed with HTP calculations for potential new SGS candidates following the

work flow shown in Fig. 1(e). In total, we have identified 80 new SGS candidates with negative formation energies. These compounds are listed in Table II along with their calculated lattice parameters, total magnetic moment, formation energy, and the distance to the convex hull data as well as the type of SGS. More detailed information can be found in the Supplemental Material [51], including elastic constants, local magnetic moments, dynamical and mechanical stability (Sec. S1), as well as band structures (Secs. S3 and S4).

Among the SGS candidates listed in Table II, 70 compounds are also mechanically and dynamically stable. Consideration of the distance to the convex hull reduces the

number of stable SGS candidates significantly. The results obtained in the previous section indicate that quaternary Heusler compounds with a distance to the convex hull  $\Delta E_{\text{con}}$  of about 0.1 eV/atom can still be synthesized. This relatively large  $\Delta E_{\text{con}}$  may be partially due to disorder effects. Among our newly predicted SGS candidates, 17 compounds have a distance to the convex hull below 0.1 eV/atom. These alloys are thus most likely to be synthesized and highlighted in Table II. CoRuCrAl, IrCoTaGa, and Co<sub>2</sub>NbX ( $X = \text{Al, Ga, and In}$ ) also have very small distances ( $<0.03$  eV/atom) to the convex hull, but are either dynamical or mechanical unstable. Such candidates may be synthesized by special experimental techniques such as the molecular beam epitaxy method.

Recent studies have shown that configuration-disorder-driven entropy can stabilize some oxides and alloys [52,53]. Similarly, CoFeCrAl with a distance to the convex hull as high as 0.1139 eV/atom can be synthesized due to Cr-Al antisite disorder [43,50]. Furthermore, disorder will also have an impact on the electronic structure. To explore this further, we performed a case study on NiFeMnAl. The total magnetic moment will be reduced by 8% for Ni(Fe<sub>0.7</sub>Mn<sub>0.3</sub>)(Mn<sub>0.7</sub>Fe<sub>0.3</sub>)Al with Fe-Mn antisite disorder. The energy bands are smeared out due to the disorder effect, but the main features of the electronic structures are still preserved. Detailed discussion of disorder effect can be found in Sec. S5 of the Supplemental Material [51].

Most of the newly predicted SGSs in Table II are quaternary Heusler compounds. We have only found three new ternary SGSs (e.g., Co<sub>2</sub>NbX,  $X = \text{Al, Ga, and In}$ ), but they are either dynamically or mechanically unstable. Among the previous predicted six ternary Heusler SGSs, only Mn<sub>2</sub>CoAl is a stable candidate. In this regard, Mn<sub>2</sub>CoAl is a special case. Our analysis on systems with the same number of valence electrons as Mn<sub>2</sub>CoAl, such as Mn<sub>2</sub>FeSi, reveals that the CBM and VBM have very strong overlap, destroying the SGS behavior. In general, the occurrence of the SGS phase depends significantly on detailed hybridization of the atomic orbitals, as discussed below. Therefore, the empirical rule on the number of electrons serves only as a qualitative guide, and explicit DFT calculations on the electronic structure are required to identify such phases. It is noteworthy that all four types of SGSs as sketched in Fig. 1(a) are represented in Table II. There are 28 (32, 9, and 1) type-I (type II, type-III, and type-IV) SGSs, respectively. In the following, we will discuss the electronic and magnetic properties for some representative cases among the 70 both mechanically and dynamically stable candidates, focusing on developing better understanding of the physical properties.

### 1. Magnetization

Essentially, SGSs are half metals; thus the total magnetic moments are expected to be integers, and they should obey the Slater-Pauling rule [10,40]. According to Table II, it is obvious that when  $N_V$  is 26 and 28, the resulting magnetic moments are  $2.0 \mu_B$  and  $4.0 \mu_B$  following  $M_{\text{tot}} = (N_V - 24) \mu_B$ , where  $M_{\text{tot}}$  and  $N_V$  are the total magnetic moment and number of valence electrons per unit cell, respectively.

For the cases with  $N_V$  being 21, the total magnetic moments are  $3.0 \mu_B$  following  $M_{\text{tot}} = (N_V - 18) \mu_B$ . This is consistent with the expected values based on the Slater-Pauling rule.

Such behaviors of the magnetization for Heusler compounds can be understood based on the atomic models, as demonstrated in previous studies [10,40]. Generally, the magnitude of the magnetic moments is caused by the competition between the crystal field splitting (between  $t_{2g}$  and  $e_g$  states) and the exchange splitting (between the majority and minority spin channels) [54–56]. In Ref. [40], a picture with bonding and antibonding  $t_{2g}$  and  $e_g$  bands is applied to interpret the quaternary Heusler compounds with one magnetic ion, due to significant hybridization between the  $d$  orbitals. Such a picture has to be generalized in order to understand the magnetization of the quaternary Heusler SGSs, especially for cases with more than one type of magnetic atom.

The  $t_{2g}$ - $e_g$  picture is valid for compounds with one magnetic ion. For instance, as shown by the density of states for PtVYAl (Fig. S1(a) in the Supplemental Material [51]), the  $t_{2g}$  states in the majority-spin channels are occupied, resulting in a total magnetization of  $3.0 \mu_B$  per formula unit. This is generally true for other cases with  $N_V = 21$ , such as XVScSn ( $X = \text{Co, Ir, and Rh}$ ), PtVYAl, and FeCrScSi. For the  $N_V = 26$  cases, the  $t_{2g}$  shells in both spin channels are filled, while the  $e_g$  state is only occupied in the majority-spin channel, leading to a total magnetization of  $2.0 \mu_B$  per formula unit, as demonstrated by IrFeTiSb Fig. S1(b) in the Supplemental Material.

The crystal field splitting changes greatly for systems with two or more magnetic ions. It is well known that for full Heusler with chemical formula  $X_2YZ$ , the site symmetry for both  $Y$  and  $Z$  is  $m\bar{3}m$  ( $O_h$ ), while that for  $X$  is  $\bar{4}3m$  ( $T_d$ ). The  $d$  shell will split into  $t_{2g}$  and  $e_g$  subshells in both  $O_h$  and  $T_d$  crystallographic symmetries [57]. For quaternary Heuslers, the site symmetry for  $X, X', Y,$  and  $Z$  sites is the same, i.e., of the  $T_d$  type. However, it is observed that the  $t_{2g}$ - $e_g$  picture is not applicable in quaternary Heusler alloys with two magnetic ions, as detailed below.

In the tetrahedral crystal field ( $T_d$  symmetry), the doubly degenerated state  $e_g$  is lower in energy than the triply degenerated  $t_{2g}$  state [58]. It is noted that the relative energy level between the  $t_{2g}$  and  $e_g$  states depends on the bonding to the neighboring atoms [56]. Furthermore, we found that the  $t_{2g}$  and  $e_g$  shells will “split” into subshells, namely,  $t_{2g} \rightarrow e'_g + b_{1g}$  and  $e_g \rightarrow a_{1g}^* + b_{1g}^*$ , as sketched in Fig. 2(a) (cf. Sec. S2.1 in the Supplemental Material [51] for a detailed discussion on the effect of chemical environment on the crystal field splitting). Taking FeVNbAl as an example, for both Fe and V atoms, as indicated by the partial density of states shown in Fig. 2(b), there are two peaks (marked as  $e'_g$  and  $b_{1g}$ ) originating from the  $t_{2g}$  orbitals, which can accommodate two and one electrons, respectively. For the  $e_g$  orbitals, the two resulting peaks are denoted as  $a_{1g}^*$  and  $b_{1g}^*$ ; each can host one electron. We want to emphasize that the  $t_{2g} \rightarrow e'_g + b_{1g}$  and  $e_g \rightarrow a_{1g}^* + b_{1g}^*$  “splitting” are not due to the lowering of the symmetry from  $T_d$  to  $D_{4h}$  but due to the strong  $d$ - $d$  hybridization as detailed below. Thus we dub it the  $D_{4h}$ -like picture. As shown in Fig. S7 in the Supplemental Material [51], the resulting  $e'_g$  and  $b_{1g}$  subshells have equal contributions from the  $d_{xy}, d_{yz},$  and  $d_{zx}$  orbitals, which is also the same for the

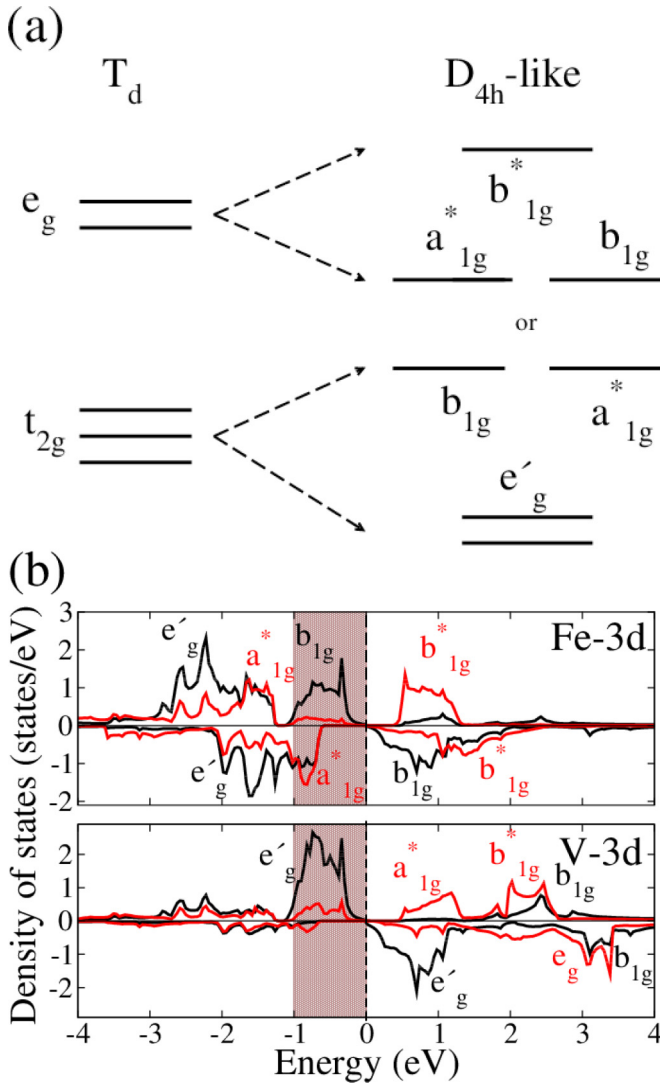


FIG. 2. (a) Sketch of crystal field splitting for magnetic atoms in typical quaternary Heusler compounds (see main text for detailed discussion). (b) Local density of states (LDOS) for Fe (upper panel) and V (lower panel) atoms in FeVNbAl. The dashed line denotes the Fermi level. The black and red curves denote the  $t_{2g}$  and  $e_g$  orbitals, respectively. The shaded region highlights the strong hybridization between the Fe- $b_{1g}$  subshell and V- $e'_g$  subshell in the majority spin channel, of which the energy range is from about  $-1$  to  $0$  eV.

$a_{1g}^*$  and  $b_{1g}^*$  subshells with equal contributions from the  $d_{x^2-y^2}$  and  $d_{3z^2-r^2}$  orbitals. In general, for the quaternary Heusler compounds, it is observed that the  $b_{1g}$  subshell originating from the  $t_{2g}$  shell can be either higher or lower in energy than the  $e_g$ -derived  $a_{1g}^*$  subshells [Figs. 2(a) and 2(b)].

Such a  $D_{4h}$ -like picture of crystal field splitting can be attributed to the bonding strength of different atomic pairs associated with the magnetic ions. For FeVNbAl, although the nearest-neighbor V-Nb bond length ( $2.64 \text{ \AA}$ ) is the same as that of the nearest-neighbor V-Al bond, the integrated COHP for the V-Nb bonds is about  $-4.04$  eV, which is much stronger than the V-Al bonding with an integrated COHP of  $-1.33$  eV. The nearest-neighbor Fe-Nb and Fe-Al bond lengths are the same ( $2.64 \text{ \AA}$ ), and also the integrated-COHP values are

comparable ( $-2.33$  eV and  $-2.07$  eV). Moreover, the next-nearest-neighbor V-Fe bond length is about  $3.05 \text{ \AA}$ , but the integrated COHP is about  $-1.62$  eV, which is comparable to that of the nearest-neighbor V-Al, Fe-Nb, and Fe-Al bonds, indicating strong bonding between next-nearest-neighbor V-Fe bonds. Such features can be clearly observed from the DOS [Fig. 2(b)], where the hybridization between the  $d$  orbitals of V and Fe is obviously strong. Such splittings of the original  $t_{2g}$  and  $e_g$  shells do not result in the separation of the  $\{d_{xy}, d_{yz}, d_{zx}\}$  (due to local tetragonal crystal fields) or  $\{d_{x^2-y^2}, d_{3z^2-r^2}\}$  (due to Jahn-Teller like distortions) orbitals (cf. Fig. S7 in the Supplemental Material [51]), like the local tetragonal distortions on the  $d$  orbitals in the octahedral environment. In contrast, the  $\{d_{xy}, d_{yz}, d_{zx}\}$  orbitals are still triply degenerated in the  $e'_g$  and  $b_{1g}$  subshells, while the  $\{d_{x^2-y^2}, d_{3z^2-r^2}\}$  orbitals are still doubly degenerated in both  $a_{1g}^*$  and  $b_{1g}^*$  subshells (cf. Fig. S7 in the Supplemental Material [51]).

Following such a splitting scheme, the resulting magnetic moments for compounds with two magnetic elements can be easily understood. For the  $N_V = 21$  cases such as FeVNbAl (cf. Fig. 2(b) and Fig. S5 in the Supplemental Material [51]), the magnetic moment of  $2.0 \mu_B$  on the V atoms is due to the  $e'_g$  subshell (which originates from  $t_{2g}$  shell) in the majority-spin channel [Fig. 2(b)]. Moreover, for the Fe atoms, the  $e'_g$ ,  $b_{1g}$ , and  $a_{1g}^*$  subshells in the majority-spin channel are occupied, while only the  $e'_g$  and  $a_{1g}^*$  subshells in the minority-spin channel are occupied, resulting in a magnetic moment of  $1.0 \mu_B$ . It is noted that in this case the  $b_{1g}$  subshells can be higher in energy than the  $a_{1g}^*$  subshells. The magnetization of other two magnetic ion compounds with  $N_V = 21$  can also be understood in a similar way (not shown).

A similar picture can also be applied to the  $N_V = 26$  cases with two magnetic ions, where the total magnetic moments of  $2.0 \mu_B$  can be attributed to  $1.0 \mu_B$  atomic moments from two atoms. Here we take CoFeTaGe (cf. Fig. S2(b) and Fig. S6 in the Supplemental Material [51]) as an example. The bond lengths of nearest-neighbor Co-Ge and Fe-Ge almost have the same value as  $2.57 \text{ \AA}$ . However the integrated COHP of Co-Ge is  $-1.62$  eV, which is larger than that of Fe-Ge ( $-1.03$  eV). Moreover, the next-nearest-neighbor Co-Fe bonds have a comparable bond length to the Co-Ge and Fe-Ge bonds (about  $2.96 \text{ \AA}$ ), but a much weaker bonding with integrated COHP as  $-0.50$  eV. The resulting crystal field splittings are very comparable to those in the cases with  $N_V = 21$  (cf. Fig. S6 in the Supplemental Material [51]). For the Co atoms, the only unoccupied state is the  $b_{1g}^*$  subshell in the minority-spin channel, whereas the majority-spin channel is fully occupied, resulting in a  $1.0 \mu_B$  magnetic moment. For the Fe atoms, the  $t_{2g}$  is not split in either spin channel and lies below the Fermi level. The  $e_g$  state is weakly split into  $a_{1g}^*$  and  $b_{1g}^*$  subshells below the Fermi level in the majority-spin channel. On the other hand, in the minority-spin channel the  $e_g$  state is split into a widespread  $a_{1g}^*$  subshell below the Fermi level and a localized  $b_{1g}^*$  above the Fermi level. So the majority-spin channel also has one more state than the minority-spin channel, resulting in one  $\mu_B$  magnetic moment (cf. Fig. S6 in the Supplemental Material).

In short, it is observed that the magnetization of quaternary Heusler compounds with two magnetic ions can be understood based on the crystal splittings of the  $D_{4h}$ -like



picture. Such splittings originate from the anisotropic bonding between the ions. In this regard, the required band filling to achieve SGSs is more flexible for quaternary Heusler compounds than the ternary cases. This explains also why we found more candidate SGSs in the quaternary Heusler systems, as mentioned above. On the other hand, as to the only new SGS (NiFeMnAl) with 28 electrons (cf. Fig. S3 in the Supplemental Material), the hybridization between  $d$  orbitals from the Ni, Fe, and Mn atoms is so strong that the atomic picture is not applicable. This is also true for the other cases with three magnetic ions.

## 2. Properties of four types of SGSs

For all four types of SGSs, the electronic structures for one representative case in each class are shown in Fig. 3, together with the AHCs and spin-resolved longitudinal conductivities. For PtVYAl, which is a type-I SGS, the VBM (at the  $\Gamma$  point) and CBM (at the  $X$  point) touch each other indirectly in the majority-spin channel, while there is a gap of about 0.6 eV in the minority-spin channel. Thus, the system is expected to show typical behavior of half metals, i.e., 100% spin-polarized transport properties. For type-II SGSs as exemplified by FeVHfSi, the VBM and CBM have the opposite spin characters and touch each other indirectly at the Fermi level [Fig. 3(b)]. In this case, the spin polarization of the resulting current can be tuned by tailoring the Fermi energy. For RuCrZrAl which represents type-III SGSs, the valence bands near the Fermi energy are mostly of the majority-spin character, while the conduction bands constitute both majority and minority spin character carriers. This is in contrast to the case of NiFeMnAl (a type-IV SGS), where the conduction bands originate from one spin channel while the valence bands have both majority and minority spin characters.

Such specific electronic structures for four types of SGSs can be reflected in the transport properties in terms of the AHC and longitudinal conductivity, shown as well in Fig. 3. Due to vanishing DOS at the Fermi energy, a common phenomenon for the four representative SGSs is that the AHC vanishes at Fermi level. That is, the indirect band gaps for such compounds are topologically trivial, i.e., there exists no quantum anomalous Hall effect. This is comparable with the experimental AHC of  $\text{Mn}_2\text{CoAl}$  (also a type-II SGS) [2]. Moreover, for type-II SGSs such as HfVFeSi, there is a sign change for the AHC around the Fermi energy, due to the fact that the spin character of the carriers changes when they are excited from VBM to CBM. The resulting derivative of the AHC is as high as 1597 S/(cm eV), corresponding to a large anomalous Nernst effect (ANE). In this sense, such type-II SGSs are likely promising candidates for engineering spintronic field-effect transistors.

The right panels of Fig. 3 display the spin-resolved longitudinal conductivities at 300 K for four types of SGSs. Like the AHC, the longitudinal conductivities of all four SGSs are quite low due to the vanishing DOS at the Fermi energy. For type-I SGSs as exemplified by PtVYAl, the conductivity mostly originates from the majority-spin channel, showing typical behavior of half metals. For type-II SGSs (FeVHfSi), due to the VBM and CBM with opposite spin characters, the spin polarization of the longitudinal conductivity can

be conveniently tuned by controlling the chemical potential. Such compounds may be used to fabricate spin valves which are switchable via electrostatic gating. In case of type-III SGSs (RuCrZrAl), above the Fermi energy the conductivity has finite values for both spin channels, while the conductivity is nonzero only for one spin channel below the Fermi energy (Fig. 3). Such transport property is opposite that of the type-IV SGSs [Fig. 3(d)]. It is an interesting question how such two types of SGSs can be utilized for future spintronic devices.

## 3. Effects of spin-orbit coupling

It is observed that SOC can induce significant changes in the electronic structure of SGSs, since the band gaps of SGSs are on average of small magnitude (cf. Sec. S4 in the Supplemental Material [51]). For instance, for IrVScSn, the indirect band gap is about 58.4 meV without SOC [Fig. 4(a)]. When SOC is turned on with magnetization direction along the [001] direction, the band gap is reduced to only 0.6 meV. Such a large change in the magnitude of the band gap can be attributed to the fact that the CBM is mainly derived from the Ir- $d$  orbitals, where the atomic SOC strength is about 0.5 eV. Such SOC effect on electronic structure is particularly associated with compounds constituted of heavy elements such as Os, Ir, and Pt, due to the strong atomic SOC strength. Similarly, it is expected that SOC has significant influence on the electronic structure for compounds with heavy elements such as Os, Ir, and Pt. This is indeed confirmed by our explicit DFT calculations for IrVScSn, IrVScSi, IrVYSn, PtVScAl, and OsCrZrAl (cf. Sec. S4 in the Supplemental Material), where the band gap size can be fine tuned by about 15 meV on average. As to OsCrYSi, the gap is even closed and the CBM and VBM are overlapping. In the following we discuss IrVScSn as an example for SOC effects on SGSs.

As the SGSs are magnetic, the combination of magnetic ordering with SOC lowers the symmetry of the systems, leading to magnetization-direction-dependent physical properties. Figure 4(c) shows the magnetization direction dependence of the band gap for IrVScSn, as the magnetization direction rotates in the (001) plane. Obviously, the magnitude of the band gap shows a continuous behavior of the sinusoidal type as a function of the azimuthal angle  $\varphi$  (the angle between the magnetization direction and the [100] axis). A maximal band gap of 14.8 meV is achieved for  $\varphi = \frac{\pi}{4}$ . Such changes in the fine structure of electronic structure can be manifested by the anisotropic magnetoresistance (AMR) effect. Using the constant relaxation time ( $\tau$ ) approximation, we estimated the AMR ratio at 300 K following the semiclassical transport theory, given by

$$\frac{\rho(0) - \rho(\frac{\pi}{4})}{\rho(0)} = \frac{\frac{1}{\sigma(0)} - \frac{1}{\sigma(\frac{\pi}{4})}}{\frac{1}{\sigma(0)}} = \frac{\frac{1}{\sigma(0)/\tau} - \frac{1}{\sigma(\frac{\pi}{4})/\tau}}{\frac{1}{\sigma(0)/\tau}}, \quad (12)$$

where  $\sigma(\varphi)$  [ $\rho(\varphi)$ ] is the longitudinal conductivity (resistivity) with the azimuthal angle  $\varphi$  for the magnetization direction in the (001) plane. This results in an AMR ratio as large as 33%. On the other hand, the magnetocrystalline anisotropy energy between such two cases with azimuthal angle  $\varphi = 0$  and  $\frac{\pi}{4}$  is only about  $10^{-6}$  eV per formula unit, due to the underlying cubic symmetry. Therefore, we suspect that such materials with large AMR ratio and easily tunable



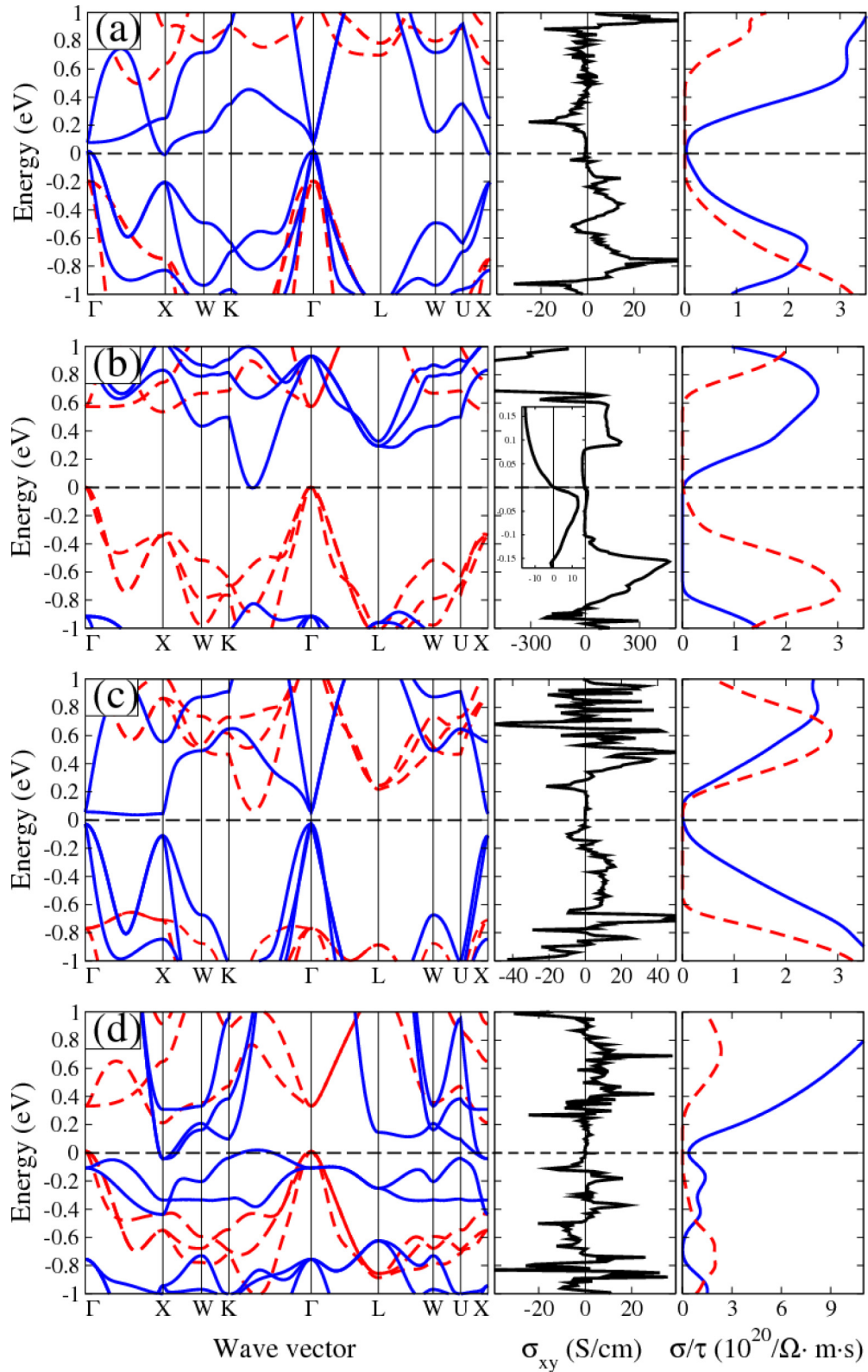


FIG. 3. (a), (b), (c), and (d) are the band structure (left), anomalous Hall conductivity (middle), and spin-resolved longitudinal conductivity (right) of PtVYAl (type I), FeVHfSi (type II), RuCrZrAl (type III), and NiFeMnAl (type IV), respectively. The inset in the middle panel of (b) displays the zoom-in of AHC  $\pm 0.17$  eV around the Fermi energy. The solid blue and dashed red lines denote the majority and minority spin channels, respectively. The horizontal dashed lines indicate the Fermi energy.

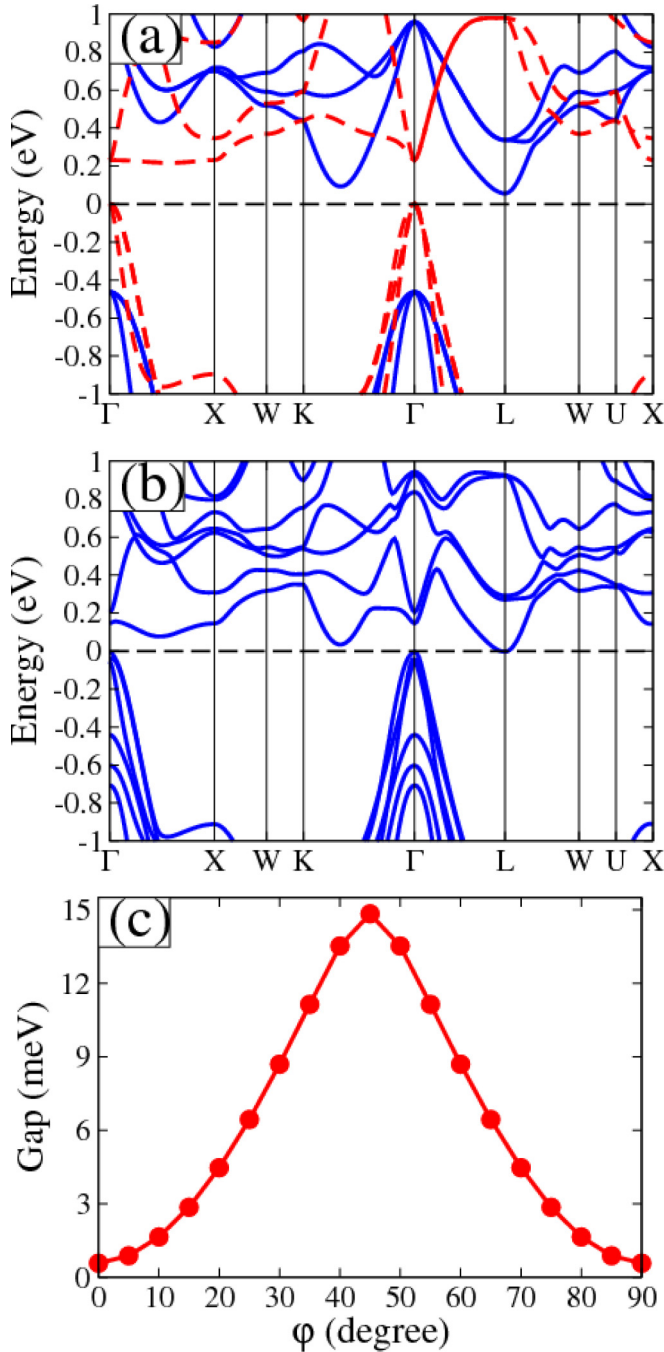


FIG. 4. (a) and (b) are the band structures of IrVScSn without and with SOC. Without SOC, the solid blue and dashed red curves are majority and minority spin channels, respectively. (c) The calculated gap as a function of azimuthal angle  $\phi$  (the angle between the magnetization direction and the [100] axis) in the (001) plane. The horizontal dashed lines indicate the Fermi energy.

magnetization directions can be applied for future spintronic applications.

#### 4. SGS with direct band touching

As shown in Fig. 5, we find NiCrMnAl is a special SGS, where a direct band touching occurs at the  $\Gamma$  point. Without considering SOC, the CBM from the minority-spin channel

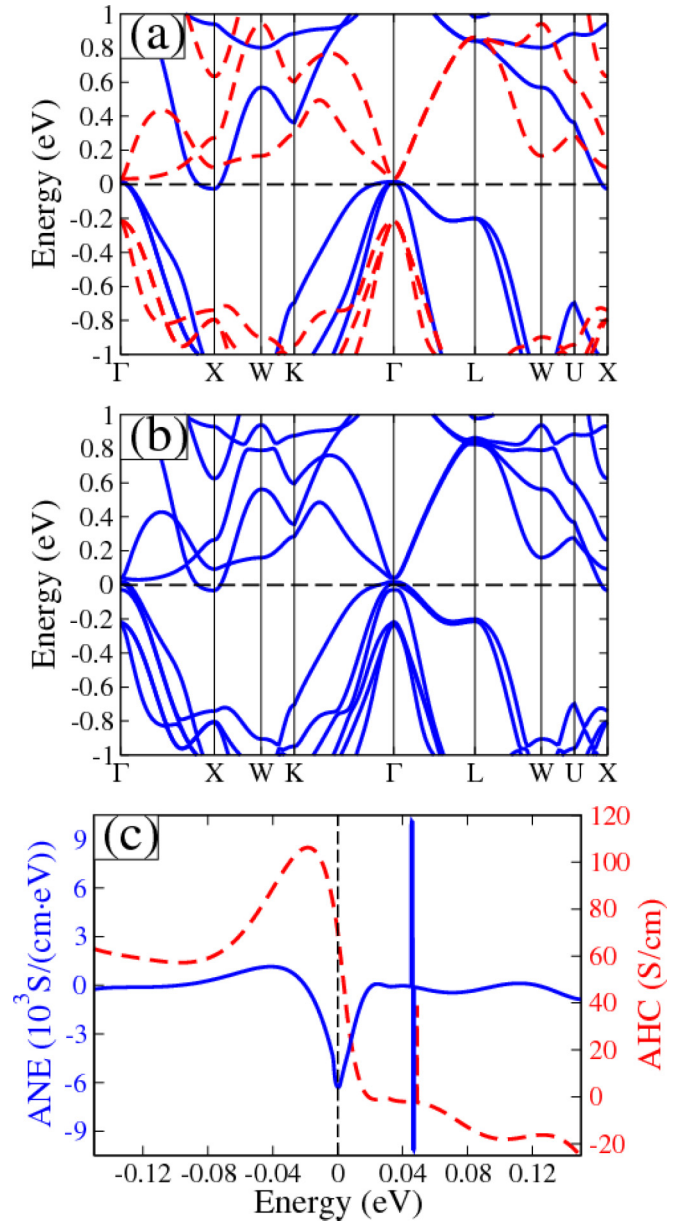


FIG. 5. (a) and (b) are the band structures of NiCrMnAl without and with SOC. Without SOC, the solid blue and dashed red curves are majority and minority spin channels, respectively. (c) The dashed red and solid blue curves are AHC and ANE results  $\pm 0.15$  eV around Fermi level, respectively. The horizontal [panels (a) and (b)] and vertical [panel (c)] dashed lines indicate the Fermi energy.

touches the VBM with the opposite spin character. That is, it is a type-II SGS following the classification discussed above. Unfortunately, due to the presence of a conduction band which goes slightly below the Fermi energy at the X point, the direct touching point is hidden. When SOC is turned on, a band gap of 24 meV is opened locally at the  $\Gamma$  point. However, the resulting band gap is topologically trivial according to the AHC shown in Fig. 5(c), since the AHC changes its sign around the Fermi energy, similarly to what we saw in the above discussions of FeVHfSi. Moreover, the AHC shows a singularity for an energy about 50 meV above the Fermi energy. This indicates there is band anticrossing in the electronic

structure. Particularly, due to the drastic variation of the AHC with respect to the chemical potential around Fermi level, the resulting derivative of the AHC is as large as  $-6000$  S/(cm eV) at the Fermi level. That is, a gigantic anomalous Nernst effect is expected in NiCrMnAl. Such a derivative of the AHC is much larger than that of the recent experimentally realized large anomalous Nernst effect in  $\text{Mn}_3\text{Sn}$  with a value of  $-845$  S/(cm eV) [59–61]. In this sense, type-II SGSs may be promising materials for anomalous Nernst applications.

#### IV. CONCLUSIONS

To summarize, we have carried out a systematic high-throughput screening for spin-gapless semiconductors (SGSs) in quaternary Heusler compounds with 21, 26, and 28 valence electrons. After validating our calculations with the previously reported cases, we predicted 80 new stable compounds (based on the formation energy) as promising candidates of spin-gapless semiconductors, where 70 cases are stable based on further evaluation of the mechanical and dynamical stabilities. The magnetization of SGSs obeys the Slater-Pauling rule, which can be interpreted based on a new scheme of crystal field splitting of the  $D_{4h}$ -like picture. Interestingly, all four types of SGSs have been identified among our candidate systems, where both the longitudinal conductivity and

transversal anomalous Hall conductivity are calculated. We find the type-II SGSs are particularly interesting for spintronic applications as the spin polarization of the longitudinal conductivity is very sensitive to the chemical potential, while the anomalous Hall conductivity changes its sign across the Fermi level, leading to a significant anomalous Nernst effect. This is also true for the SGS candidate NiCrMnAl with direct touching. Additionally, it is also demonstrated that spin-orbit coupling can have significant effect on the electronic structure of SGSs with heavy elements, where the band gap can be tuned by the magnetization direction, resulting in a large anisotropic magnetoresistance in cubic crystals. Therefore, we suspect that SGSs are promising materials for future spintronic applications, awaiting further experimental and theoretical explorations.

All the data are freely available in the Novel Materials Discovery (NOMAD) Laboratory [62].

#### ACKNOWLEDGMENTS

Q.G. acknowledges financial support from the China Scholarship Council. The authors gratefully acknowledge computational time on the Lichtenberg High Performance Supercomputer.

- 
- [1] X. L. Wang, *Phys. Rev. Lett.* **100**, 156404 (2008).
- [2] S. Ouardi, G. H. Fecher, C. Felser, and J. Kübler, *Phys. Rev. Lett.* **110**, 100401 (2013).
- [3] M. Wang, R. P. Campion, A. W. Rushforth, K. W. Edmonds, C. T. Foxon, and B. L. Gallagher, *Appl. Phys. Lett.* **93**, 132103 (2008).
- [4] S. Skaftouros, K. Özdoğan, E. Şaşıoğlu, and I. Galanakis, *Appl. Phys. Lett.* **102**, 022402 (2013).
- [5] G. Z. Xu, E. K. Liu, Y. Du, G. J. Li, G. D. Liu, W. H. Wang, and G. H. Wu, *Europhys. Lett.* **102**, 17007 (2013).
- [6] G. Y. Gao and K. L. Yao, *Appl. Phys. Lett.* **103**, 232409 (2013).
- [7] W. Feng, X. Fu, C. Wan, Z. Yuan, X. Han, N. V. Quang, and S. Cho, *Phys. Status Solidi RRL* **9**, 641 (2015).
- [8] L. Bainsla, A. I. Mallick, M. M. Raja, A. K. Nigam, B. S. D. C. S. Varaprasad, Y. K. Takahashi, A. Alam, K. G. Suresh, and K. Hono, *Phys. Rev. B* **91**, 104408 (2015).
- [9] M. E. Jamer, B. A. Assaf, G. E. Sterbinsky, D. Arena, L. H. Lewis, A. A. Saul, G. Radtke, and D. Heiman, *Phys. Rev. B* **91**, 094409 (2015).
- [10] Q. Gao, H. H. Xie, L. Li, G. Lei, J. B. Deng, and X. R. Hu, *Superlattice Microstruct.* **85**, 536 (2015).
- [11] X. T. Wang *et al.*, *J. Mater. Chem. C* **4**, 7176 (2016).
- [12] X. L. Wang, *Natl. Sci. Rev.* **3**, 252 (2016).
- [13] S. Curtarolo, G. L. W. Hart, M. Buongiorno Nardelli, N. Mingo, S. Sanvito, and O. Levy, *Nat. Mater.* **12**, 191 (2013).
- [14] I. Opahle, A. Parma, E. J. McEniry, R. Drautz, and G. K. H. Madsen, *New J. Phys.* **15**, 105010 (2013).
- [15] J. Carrete, W. Li, N. Mingo, S. Wang, and S. Curtarolo, *Phys. Rev. X* **4**, 011019 (2014).
- [16] J. G. He, M. Amsler, Y. Xia, S. S. Naghavi, V. I. Hegde, S. Hao, S. Goedecker, V. Ozolins, and C. Wolverton, *Phys. Rev. Lett.* **117**, 046602 (2016).
- [17] J. G. He *et al.*, [arXiv:1802.04875](https://arxiv.org/abs/1802.04875).
- [18] J. Ma, J. He, D. Mazumdar, K. Munira, S. Keshavarz, T. Lovorn, C. Wolverton, A. W. Ghosh, and W. H. Butler, *Phys. Rev. B* **98**, 094410 (2018).
- [19] S. Sanvito *et al.*, *Sci. Adv.* **3**, 1602241 (2017).
- [20] J. Balluff, K. Diekmann, G. Reiss, and M. Meinert, *Phys. Rev. Mater.* **1**, 034404 (2017).
- [21] S. V. Faleev, Y. Ferrante, J. Jeong, M. G. Samant, B. Jones, and S. S. P. Parkin, *Phys. Rev. Appl.* **7**, 034022 (2017).
- [22] Y. Venkateswara, S. Gupta, S. S. Samatham, M. R. Varma Enamullah, K. G. Suresh, and A. Alam, *Phys. Rev. B* **97**, 054407 (2018).
- [23] P. Klaer, B. Balke, V. Alijani, J. Winterlik, G. H. Fecher, C. Felser, and H. J. Elmers, *Phys. Rev. B* **84**, 144413 (2011).
- [24] X. P. Wei, Y. L. Zhang, Y. D. Chu, X. W. Sun, T. Sun, P. Guo, and J. B. Deng, *J. Phys. Chem. Solids* **82**, 28 (2015).
- [25] V. Alijani *et al.*, *Phys. Rev. B* **84**, 224416 (2011).
- [26] I. Opahle, G. K. H. Madsen, and R. Drautz, *Phys. Chem. Chem. Phys.* **14**, 16197 (2012).
- [27] G. Kresse and J. Furthmüller, *Phys. Rev. B* **54**, 11169 (1996).
- [28] G. Kresse and D. Joubert, *Phys. Rev. B* **59**, 1758 (1999).
- [29] D. Vanderbilt, *Phys. Rev. B* **41**, 7892(R) (1990).
- [30] J. P. Perdew, J. A. Chevary, S. H. Vosko, K. A. Jackson, M. R. Pederson, D. J. Singh, and C. Fiolhais, *Phys. Rev. B* **46**, 6671 (1992).
- [31] J. P. Perdew, K. Burke, and M. Ernzerhof, *Phys. Rev. Lett.* **77**, 3865 (1996).
- [32] J. E. Saal, S. Kirklin, M. Aykol, B. Meredig, and C. Wolverton, *JOM* **65**, 1501 (2013).
- [33] K. Koepnik and H. Eschrig, *Phys. Rev. B* **59**, 1743 (1999).
- [34] I. Opahle, K. Koepnik, and H. Eschrig, *Phys. Rev. B* **60**, 14035 (1999).
- [35] M. Born and K. Huang, *Dynamics Theory of Crystal Lattices* (Oxford University Press, 1954).

- [36] A. Togo and I. Tanaka, *Scr. Mater.* **108**, 1 (2015).
- [37] A. A. Mostofi, J. R. Yates, Y. S. Lee, I. Souza, D. Vanderbilt, and N. Marzari, *Comput. Phys. Commun.* **178**, 685 (2008).
- [38] G. K. H. Madsen and D. J. Singh, *Comput. Phys. Commun.* **175**, 67 (2006).
- [39] V. L. Deringer, A. L. Tchougreeff, and R. Dronskowski, *J. Phys. Chem. A* **116**, 21 (2011).
- [40] K. Özdoğan, E. Şaşıoğlu, and I. Galanakis, *J. Appl. Phys.* **113**, 193903 (2013).
- [41] X. Yang, X. Wu, B. Wu, Y. Feng, P. Li, and H. Huang, *Mater. Sci. Eng. B* **209**, 45 (2016).
- [42] N. Xing, H. Li, J. Dong, R. Long, and C. Zhang, *Comput. Mater. Sci.* **42**, 600 (2008).
- [43] J. Nehra, V. D. Sudheesh, N. Lakshmi, and K. Venugopalan, *Phys. Status Solidi RRL* **7**, 289 (2013).
- [44] G. Y. Gao, L. Hu, K. L. Yao, B. Luo, and N. Liu, *J. Alloy. Compd.* **551**, 539 (2013).
- [45] L. Bainsla, A. I. Mallick, M. M. Raja, A. A. Coelho, A. K. Nigam, D. D. Johnson, A. Alam, and K. G. Suresh, *Phys. Rev. B* **92**, 045201 (2015).
- [46] X. Dai, G. Liu, G. H. Fecher, C. Felser, Y. Li, and H. Liu, *J. Appl. Phys.* **105**, 07E901 (2009).
- [47] H. Z. Luo, Y. P. Xin, B. H. Liu, F. B. Meng, H. Y. Liu, E. K. Liu, and G. H. Wu, *J. Alloy. Compd.* **665**, 180 (2016).
- [48] Y. J. Zhang, Z. H. Liu, E. K. Liu, G. D. Liu, X. Q. Ma, and G. H. Wu, *Europhys. Lett.* **111**, 37009 (2015).
- [49] K. Kim, L. Ward, J. G. He, A. Krishna, A. Agrawal, P. Voorhees, and C. Wolverton, Accelerated discovery of quaternary Heusler with high-throughput density functional theory and machine learning; paper presented at APS March Meeting 2018, March 5-9, 2018, Los Angeles, California.
- [50] L. Bainsla, M. M. Raja, A. K. Nigam, B. S. D. C. S. Varaprasad, Y. K. Takahashi, K. G. Suresh, and K. Hono, *J. Phys. D: Appl. Phys.* **48**, 125002 (2015).
- [51] See Supplemental Material at <http://link.aps.org/supplemental/10.1103/PhysRevMaterials.3.024410> for the atomic resolved moments, elastic constants, mechanical and dynamical stability, orbital-resolved density of states, and the band structures for the newly predicted SGS candidates, as well as discussions on the effect of disorder for NiFeMnAl.
- [52] C. M. Rost, E. Sachet, T. Borman, A. Moballeggh, E. C. Dickey, D. Hou, J. L. Jones, S. Curtarolo, and J. P. Maria, *Nat. Commun.* **6**, 8485 (2015).
- [53] Y. Lederer, C. Toher, K. S. Vecchio, and S. Curtarolo, *Acta Mater.* **159**, 364 (2018).
- [54] C. Felser, L. Wollmann, S. Chadov, G. H. Fecher, and S. S. P. Parkin, *APL Mater.* **3**, 041518 (2015).
- [55] L. Wollmann, A. K. Nayak, S. S. Parkin, and C. Felser, *Annu. Rev. Mater. Res.* **47**, 247 (2017).
- [56] T. Graf, C. Felser, and S. S. P. Parkin, *Prog. Solid State Chem.* **39**, 1 (2011).
- [57] I. Galanakis, P. H. Dederichs, and N. Papanikolaou, *Phys. Rev. B* **66**, 174429 (2002).
- [58] G. L. Miessler, P. J. Fischer, and D. A. Tarr, *Inorganic Chemistry*, 5th ed. (Pearson Education Press, 2012), p. 381.
- [59] G. Y. Guo and T. C. Wang, *Phys. Rev. B* **96**, 224415 (2017).
- [60] X. K. Li, L. C. Xu, L. C. Ding, J. H. Wang, M. S. Shen, X. F. Lu, Z. W. Zhu, and K. Behnia, *Phys. Rev. Lett.* **119**, 056601 (2017).
- [61] M. Ikhlas, T. Tomita, T. Koretsune, M. T. Suzuki, D. N. Hamane, R. Arita, Y. Otani, and S. Nakatsuji, *Nat. Phys.* **13**, 1085 (2017).
- [62] NOMAD: Novel Materials Discovery, <https://repository.nomad-coe.eu> (please search for the data using the author name “Qiang Gao”).